A sensitive and specific nanosensor for monitoring extracellular potassium levels in the brain

Jianan Liu [1,2,13], Fangyuan Li [3,4,5,13], Yi Wang [6,13], Limin Pan [7,13], Peihua Lin[3,4], Bo Zhang[8], Yanrong Zheng[6], Yingwei Xu[6], Hongwei Liao[3,4], Giho Ko[1,2], Fan Fei[6], Cenglin Xu[6], Yang Du[3,4], Kwangsoo Shin[1,2], Dokyoon Kim[1,9], Sung-Soo Jang[10], Hee Jung Chung[10], He Tian [11], Qi Wang [8], Wei Guo [12], Jwa-Min Nam[7], Zhong Chen [3,6*], Taeghwan Hyeon [1,2*] and Daishun Ling [3,4,5*]

Extracellular potassium concentration affects the membrane potential of neurons, and, thus, neuronal activity. Indeed, alterations of potassium levels can be related to neurological disorders, such as epilepsy and Alzheimer's disease, and, therefore, selectively detecting extracellular potassium would allow the monitoring of disease. However, currently available optical reporters are not capable of detecting small changes in potassium, in particular, in freely moving animals. Furthermore, they are susceptible to interference from sodium ions. Here, we report a highly sensitive and specific potassium nanosensor that can monitor potassium changes in the brain of freely moving mice undergoing epileptic seizures. An optical potassium indicator is embedded in mesoporous silica nanoparticles, which are shielded by an ultrathin layer of a potassium-permeable membrane, which prevents diffusion of other cations and allows the specific capturing of potassium ions. The shielded nanosensor enables the spatial mapping of potassium ion release in the hippocampus of freely moving mice.

Technologies for monitoring neuronal activities have long been desired to understand the mysterious function of the brain and the underlying mechanisms of neurological disorders such as epilepsy and Alzheimer's disease[1–5]. In that respect, potassium ion (K^+), as a key determinant of membrane potential[6], has been one of the main investigation targets because its concentration change in extracellular space directly affects the membrane potential of the neurons and impacts the neuronal intrinsic excitability and synaptic transmission[7–10]. Hence, there has been much effort to develop K^+ sensors that have high sensitivity and selectivity. Until recently, K^+-selective microelectrodes have been considered gold standards that allow us to measure extracellular K^+ concentration ($[K^+]_o$) with high temporal resolution[11]. Despite many advantages, such invasive electrophysiological measurements can only be used for single-point measurements of fixed samples, such as brain slices[12,13] or head-fixed animals[14,15], and are generally not applicable to freely moving animals. Alternatively, non-invasive fluorescence detection of $[K^+]_o$ holds the potential to convey the spatial and temporal information about $[K^+]_o$, manifesting itself as a promising candidate to unravel the complex neural interactions at multiple scales in the brain.

The currently available optical K^+ sensors[16,17] so far allow the routine measurements of spatiotemporal dynamics of $[K^+]_o$ in cultured cells[18], mouse brain slices[19] and anesthetized animals[20,21]. Because animal motion reflects the state of the brain, imaging $[K^+]_o$ dynamics in awake and freely moving animals is imperative for direct comparative analyses of their behaviours and neural activities. However, these K^+ sensors have yet to be realized due to the following limitations. First, the maximum ratio of $[K^+]_o$ change during action potential firing is only tenfold, from 3 to 30 mM. In comparison, the global change in intracellular calcium concentration ($[Ca^{2+}]_i$) can be as high as 10^4-fold. The existing optical K^+ sensors are not sensitive enough to detect such a small $[K^+]_o$ change. Second, despite the significant efforts to improve the selectivity of K^+ reporters[22,23], they are still far from satisfactory in differentiating K^+ from sodium ion (Na^+). This is problematic especially during action potential generation and termination when Na^+ influx is shortly followed by K^+ efflux.

In this study, we report a highly sensitive and selective K^+ nanosensor that can monitor the changes of $[K^+]_o$ in the brain of freely moving mice. We achieved the sensitive optical readout of $[K^+]_o$ changes by incorporating commercially available K^+ indicators (Asante Potassium Green-2 tetramethylammonium (TMA+) salt, APG; Supplementary Fig. 1)[24] into mesoporous silica nanoparticles (MSNs)[25–27] and subsequently shielding the MSNs with a precisely

[1]Center for Nanoparticle Research, Institute for Basic Science (IBS), Seoul, Republic of Korea. [2]School of Chemical and Biological Engineering, and Institute of Chemical Processes, Seoul National University, Seoul, Republic of Korea. [3]College of Pharmaceutical Sciences, Zhejiang University, Hangzhou, China. [4]Hangzhou Institute of Innovative Medicine, College of Pharmaceutical Science, Zhejiang University, Hangzhou, China. [5]Key Laboratory of Biomedical Engineering of the Ministry of Education, College of Biomedical Engineering & Instrument Science, Zhejiang University, Hangzhou, China. [6]Key Laboratory of Medical Neurobiology of the Ministry of Health of China, Department of Pharmacology, School of Medicine, Zhejiang University, Hangzhou, China. [7]Department of Chemistry, Seoul National University, Seoul, Republic of Korea. [8]Department of Chemistry, Zhejiang University, Hangzhou, China. [9]Department of Bionano Engineering and Bionanotechnology, Hanyang University, Ansan, Republic of Korea. [10]Department of Molecular and Integrative Physiology, University of Illinois at Urbana-Champaign, Urbana, IL, USA. [11]Center of Electron Microscope, State Key Laboratory of Silicon Material, School of Material Science and Engineering, Zhejiang University, Hangzhou, China. [12]CAS Key Laboratory of Bio-Inspired Materials and Interfacial Science, Technical Institute of Physics and Chemistry, Chinese Academy of Sciences, Beijing, China. [13]These authors contributed equally: Jianan Liu, Fangyuan Li, Yi Wang, Limin Pan. *e-mail: chenzhong@zju.edu.cn; thyeon@snu.ac.kr; lingds@zju.edu.cn

controlled thin layer of three-dimensional tripodal ligands[28]. The ligands constitute a K$^+$-specific filter membrane (Fig. 1a) that contains a binodal 3,6-connected network with a pyrite topology. The pores (~5.7 Å in diameter) of the network allow only K$^+$ (~2.66 Å in diameter[29]) to diffuse into and out of the mesopores (Fig. 1b,c).

The thicknesses of the membranes on previously reported biomimetic nanopores are typically in the order of several micrometres[30]. Here, on the other hand, we developed a synthetic approach to control the membrane thickness for shielding the MSN cores (~30 nm in diameter) completely with a thin filter layer (from 1.5 to 17.0 nm in thickness). Transmission electron microscopy (TEM) images of the nanosensors show the uniform thickness of the thin membrane filter covering the MSNs (Fig. 1d and Supplementary Fig. 2), which is further confirmed by energy-dispersive X-ray spectroscopy elemental line scan across a representative MSN (Fig. 1e). Unless otherwise indicated, all of the data were obtained using the nanosensors with a shell thickness of 3.5 nm. Additional characterization data in Supplementary Figs. 3–5 demonstrate the high yield of the core/shell structured nanosensor formation. The surface of the nanosensors was further grafted with poly(ethylene glycol) to improve their colloidal stability and biocompatibility (Supplementary Figs. 6 and 7).

The fluorescence intensity of the shielded nanosensors was sensitive only to K$^+$, whereas addition of other cations resulted in no obvious fluorescence intensity change under neutral (pH = 7.4) environment (Fig. 1f). Under mildly acidic (pH = 6.0) or basic (pH = 9.0) environment, the shielded nanosensors showed a slight decline in their signal, but still retained their superior selectivity to other metal ions. In contrast, for the unshielded nanosensors, both [K$^+$] and [Na$^+$] at 150 mM could induce significant increases in the fluorescence intensity. The K$^+$-to-Na$^+$ selectivity ratio of the unshielded nanosensors was estimated to be 2.6, while the ratio for the shielded nanosensors was 18.3. Next, we prepared another type of nanosensor containing Na$^+$ indicator, sodium-binding benzofuran isophthalate, but with the K$^+$-specific filter membrane. These obtained nanosensors did not produce any measurable response to Na$^+$ even when [Na$^+$] reached 150 mM (Supplementary Fig. 8). Collectively, these results indicate that the superior K$^+$ selectivity of the shielded nanosensors is attributed to the filter membrane that excludes the passage of ions other than K$^+$.

Compared with free K$^+$ indicators, the shielded nanosensors showed enhanced changes in fluorescence intensity when [K$^+$] increased from 0 to 150 mM (Fig. 1g). The fluorescence intensity of the nanosensors reduced almost back to the baseline when [K$^+$] decreased from 150 to 0 mM. There was no significant difference in the calibration when the nanosensors were dispersed in solutions with increasing or decreasing [K$^+$], showing that the nanosensors are fully reversible. The detection limit of the shielded nanosensors reached as low as 1.3×10^{-6} M [K$^+$] (Supplementary Fig. 9), capable of accommodating submillimolar variations of [K$^+$] in biological systems. It is noteworthy that this membrane-shielding strategy also enhanced the sensitivity and selectivity of another K$^+$ indicator, potassium-binding benzofuran isophthalate, demonstrating its versatility (Supplementary Fig. 10).

The recycling performance of the nanosensors was assessed by measuring their fluorescence signal under successive K$^+$-rich (150 mM) and K$^+$-free (0 mM) conditions for 20 cycles. As shown in Fig. 1h, the fluorescence signal variation between the K$^+$-rich and K$^+$-free conditions decreased by ~36.4% over the first six cycles and plateaued after ten cycles. This phenomenon probabably occurs due to the small quantity of remaining K$^+$ adsorbed inside the nanosensors even after external K$^+$ ions are depleted.

The fast response kinetics of the nanosensors are essential for sensing dynamic changes in [K$^+$] (ref. [31]). We evaluated the response kinetics by monitoring the fluorescence intensity changes of the shielded or unshielded nanosensors on increasing or decreasing

[K$^+$] (Fig. 1i). The measured time intervals for half-maximum K$^+$ absorption inside and desorption from the shielded nanosensors were 0.58 ± 0.14 s and 1.13 ± 0.19 s, respectively. In sharp contrast, it took about 2.81 ± 0.73 s and 2.93 ± 0.58 s for the unshielded nanosensors. These results indicate that the filter membrane with many K$^+$ affinity sites significantly contributes to the fast kinetics of the shielded nanosensors, rendering them an efficient tool for K$^+$-dependent molecular-level imaging on the second time scale.

We also investigated whether the shell thickness affects the nanosensor performance. The shell thickness was accurately controllable by varying the incubation time of the filter membrane precursors during the fabrication process. As the shell thickness increased from 1.5 to 17.0 nm, both the sensitivity and the selectivity of the nanosensors were greatly improved at the expense of their response kinetics (Supplementary Fig. 11). Considering such a trade-off, we chose the nanosensors with 3.5-nm shell thickness for in vitro and in vivo experiments.

Origin of the high sensitivity and selectivity

The pore size and composition of the filter membrane layer were revealed to play an important role in selectively capturing K$^+$ in the atomic level. While the ionic diameters of free Na$^+$ and K$^+$ are ~1.90 Å and ~2.66 Å, respectively, the diameters of hydrated Na$^+$ and K$^+$ increase to ~7.16 Å and ~6.62 Å (ref. [32]) (Fig. 2a). These sizes are still smaller than the pore size (3 nm) of the MSNs so that both hydrated Na$^+$ and hydrated K$^+$ can freely diffuse into the unshielded nanosensors. Indeed, the comparable levels of Na$^+$ and K$^+$ ions were detected inside the unshielded nanosensors after their dispersion in an aqueous solution with both 150 mM Na$^+$ and 150 mM K$^+$ (Fig. 2b). However, for shielded nanosensors, the amount of Na$^+$ inside the MSNs was negligible, indicating that Na$^+$ ions were excluded by the filter membrane (Fig. 2c). When the K$^+$-saturated shielded nanosensors were redispersed in deionized water, the K$^+$ signal inside the nanosensors diminished (Supplementary Fig. 12), further confirming the reversibility of the nanosensors.

Calculation of the interatomic distances between the atoms in the filter membrane layer shows that the size of the pore opening lined by six carbonyl oxygen atoms is ~5.7 Å, which is smaller than the diameters of the hydrated Na$^+$ and K$^+$ ions. Therefore, to pass through the membrane filter, both Na$^+$ and K$^+$ must first shed their hydration shell. After the shedding of the hydration shell, K$^+$ and Na$^+$ ions are required to interact effectively with the six carbonyl oxygen atoms at the pore entrance. Therefore, we carried out molecular dynamics simulations to investigate how the filter membrane interacts with the dehydrated K$^+$ ions (Supplementary Videos 1 and 2).

The coordination numbers for an Na$^+$ or K$^+$ ion in water were estimated to be ~5 and ~6, respectively[33,34]. When a K$^+$ ion was located at the filter membrane pore, K-O bond length was calculated to be ~2.65 Å, which is very close to the pore radius (~2.85 Å). Energy-dispersive spectroscopy (EDS) elemental mapping data of the filter membrane show that the signals from K atoms are distributed closely to those from the O atoms (Fig. 2d). These observations are in good agreement with the molecular dynamics simulation results, which indicate that the six carbonyl oxygen atoms at the membrane pore can easily replace the oxygen atoms of the six coordinating water molecules at an optimal distance by acting as surrogate water molecules (Fig. 2e). Consequently, a K$^+$ ion precisely fits in the filter membrane pore with well-balanced energetic costs and gains, which is similar to the condition proposed in the working principal of the K$^+$ channel[35,36]. However, for Na$^+$ ions, the estimated Na-O bond length (~2.18 Å) is much smaller than the membrane pore radius. After removing three coordinated water molecules when a hydrated Na$^+$ ion attaches to the surface of the filter membrane, the distance between the Na$^+$ ion and other carbonyl oxygen atoms on the other side of the pore is much larger than the optimal length when the Na$^+$
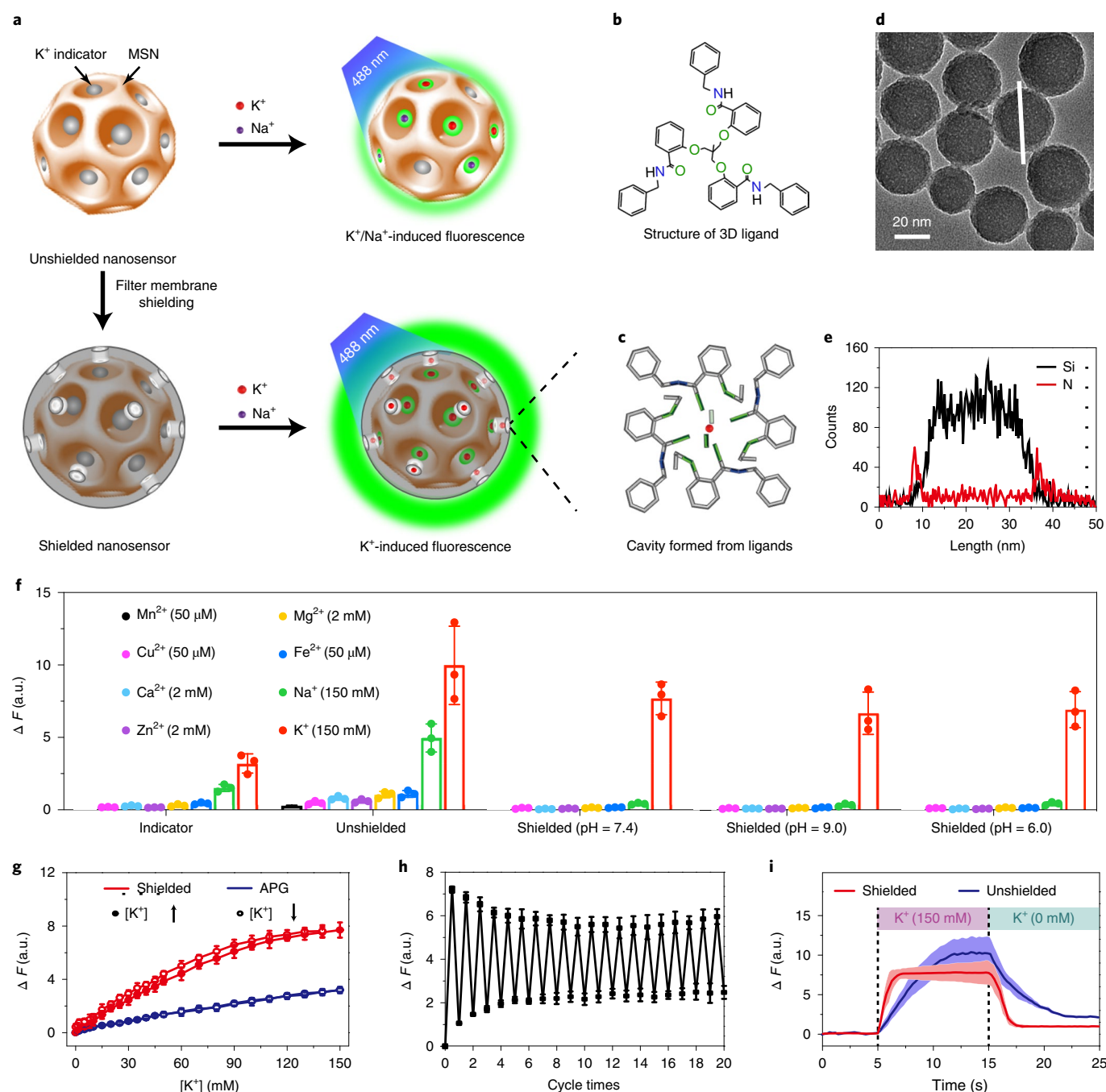
Fig. 1 | Atom-level design and performance of the K+ nanosensors. a, Schematic showing the design of the K+ nanosensor. K+ indicators are incorporated inside the MSN. The thin K+-specific filter membrane on the surface of the MSN allows only K+ to internalize into the MSN. **b**, Chemical structure of the three-dimensional ligand in the filter membrane. **c**, Chemical structure of the filter membrane whose pores are filled with K+. K atoms, red; C atoms, grey; O atoms, green; N atoms, blue. **d**, Representative TEM image of the shielded nanosensors shows the filter membrane-covered surface of the MSNs. **e**, EDS elemental line scanning profile along the white line in **d** reveals the elemental distribution and confirms the structure of the shielded nanosensor. Experiments were repeated three times independently. **f**, Graph showing that the shielded nanosensors are highly selective towards 150 mM [K+] under the neutral environment. However, a slight decline in fluorescence intensity was observed in acidic or basic environments. No significant change in fluorescence intensity was seen on the addition of other physiological cations. $\Delta F = F - F_0$, where F is the fluorescence intensity at a given ion concentration and F_0 is the fluorescence intensity at 0 mM [K+]. Data are presented as mean ± s.e.m. ($n = 3$). **g**, Changes in the fluorescence intensity of the nanosensors in response to [K+] increase from 0 to 150 mM and [K+] decrease from 150 to 0 mM. Data are presented as mean ± s.e.m. ($n = 3$). **h**, Fluorescent emission responses of the shielded nanosensors undergoing 20 cycles of incubation in K+-rich (150 mM [K+]) and K+-free (0 mM [K+]) aqueous solutions. The fluorescence change for each cycle decreases slightly over the first six cycles before reaching a plateau. Data are presented as mean ± s.e.m. ($n = 3$). **i**, Time-dependent changes in the nanosensor fluorescence intensity on the incubation in K+-rich and K+-free aqueous solutions. The shading denotes a measure of error ($n = 3$). a.u., arbitrary unit; 3D, three-dimensional.
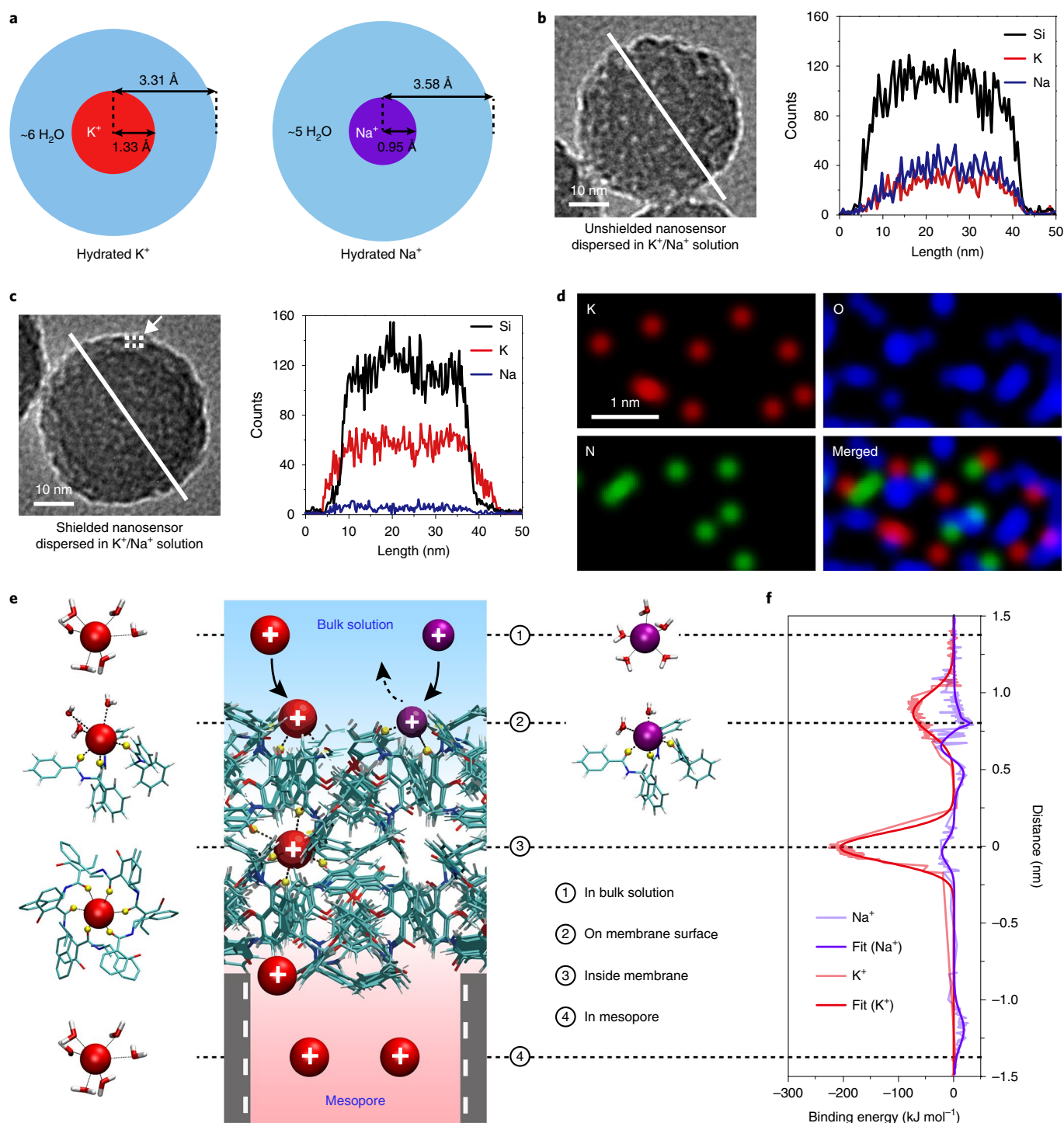
Fig. 2 | Mechanistic studies on the high selectivity and sensitivity of the shielded nanosensors. a, Schematic illustrations showing the hydration shells on K+ and Na+ in deionized water. **b,c**, Left, TEM images of unshielded nanosensor (**b**) and shielded nanosensor (**c**) dispersed in a solution containing K+ and Na+. Right, EDS elemental line scanning profiles along the white lines shown in the TEM images. **d**, EDS elemental mapping of the area in **c** marked with the dotted white box, as indicated by the white arrow. Experiments in **b–d** were repeated three times independently. **e**, Schematic illustrations of the interactions between the filter membrane cavity and K+/Na+. After shedding its hydration layer, K+ interacts with the oxygen atoms in the pore, which makes it energetically favourable for K+ to pass through the pore; however, this process is energetically unfavourable for the smaller Na+, which cannot fully interact with the oxygen atoms in the pore. **f**, Calculated binding energy between the filter membrane and K+/Na+ on dragging K+/Na+ through the filter membrane.

ion further penetrates into the pore centre. As a result, dehydration of water molecules is not complete at the membrane pore, leaving two water molecules remaining near the Na+ ion (Fig. 2e).

The binding energy of K+ or Na+ ion to the pore while passing through the membrane was determined by artificially dragging an ion through the filter membrane (Fig. 2f). Attractive effects between
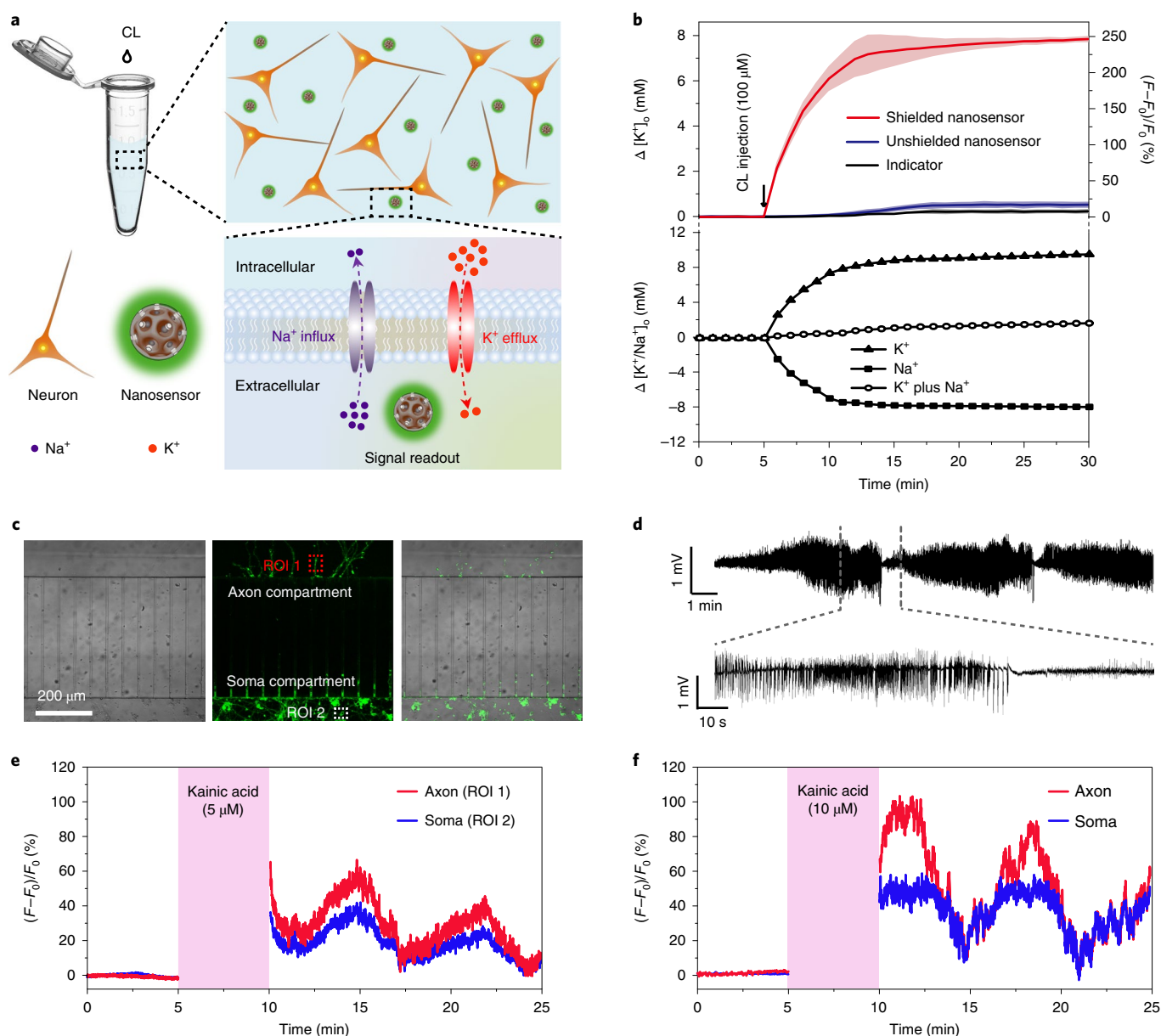
Fig. 3 | Imaging of K$^+$ release in cultured neurons. a, Experimental scheme for imaging pharmacologically modulated K$^+$ release by hippocampal neurons in aCSF. **b**, Upper, cultured hippocampal neurons were first preincubated with various sensors. On exposure to *Coriaria* lactone, fluorescence intensity of the shielded nanosensors increased, whereas no significant change was observed for the unshielded nanosensors and free indicators. Note that the left y axis is only applicable to the shielded nanosensor. Below, inductively coupled plasma measurement data for the real changes in $[K^+]_o$ and $[Na^+]_o$. The shading denotes a measure of error ($n=3$ biologically independent cultures). **c**, Representative CLSM images of the shielded nanosensor-labelled neurons cultured in a two-compartmentalized microchamber connected by microchannels. Note that the somas and axons were kept separated in two compartments. Experiments were repeated three times independently. **d**, Typical EEG data recorded from the hippocampus of a mouse which display kainic acid-induced seizures and an enlarged view for the range indicated by the dotted lines. The data are representative of three independent experiments. **e**, Fluorescence changes for the two selected areas in **c** before and after the incubation with 5 μM of kainic acid ($n=3$ biologically independent cultures). **f**, Fluorescence changes when increasing the concentration of kainic acid to 10 μM ($n=3$ biologically independent cultures). CL, *Coriaria* lactone; ROI, region of interest.

the K$^+$ ion and the filter membrane are obvious both at the surface and at the pore of the filter membrane. In sharp contrast, the Na$^+$ ion is repelled from the surface of the filter membrane and significantly less attracted by the pore. X-ray photoelectron spectroscopy data for the shielded nanosensors obtained before and after dispersion into an Na$^+$- and K$^+$-containing aqueous solution clearly show the appearance of K2p$_{3/2}$ and K2p$_1$ binding-energy peaks and no obvious change in Na1s signal (Supplementary Fig. 13), indicating that only K$^+$ ions can interact with the filter membrane.

When K$^+$-free shielded nanosensors were immersed in a K$^+$-rich solution, both electrostatic attraction and inward diffusional force facilitated the influx of K$^+$ ions into the MSNs (Supplementary Fig. 14). The diffusional flux was demonstrated to be proportional to the $[K^+]$ gradient (Supplementary Fig. 15), indicating that such a diffusion process strictly follows Fick's first law. When $[K^+]$ of the solution ($[K^+]_{out}$) is equal to $[K^+]$ in the MSNs ($[K^+]_{in}$), there is still a net influx of K$^+$ ions due to the contribution by the electrostatic attractive force even in the absence of net diffusional flux.
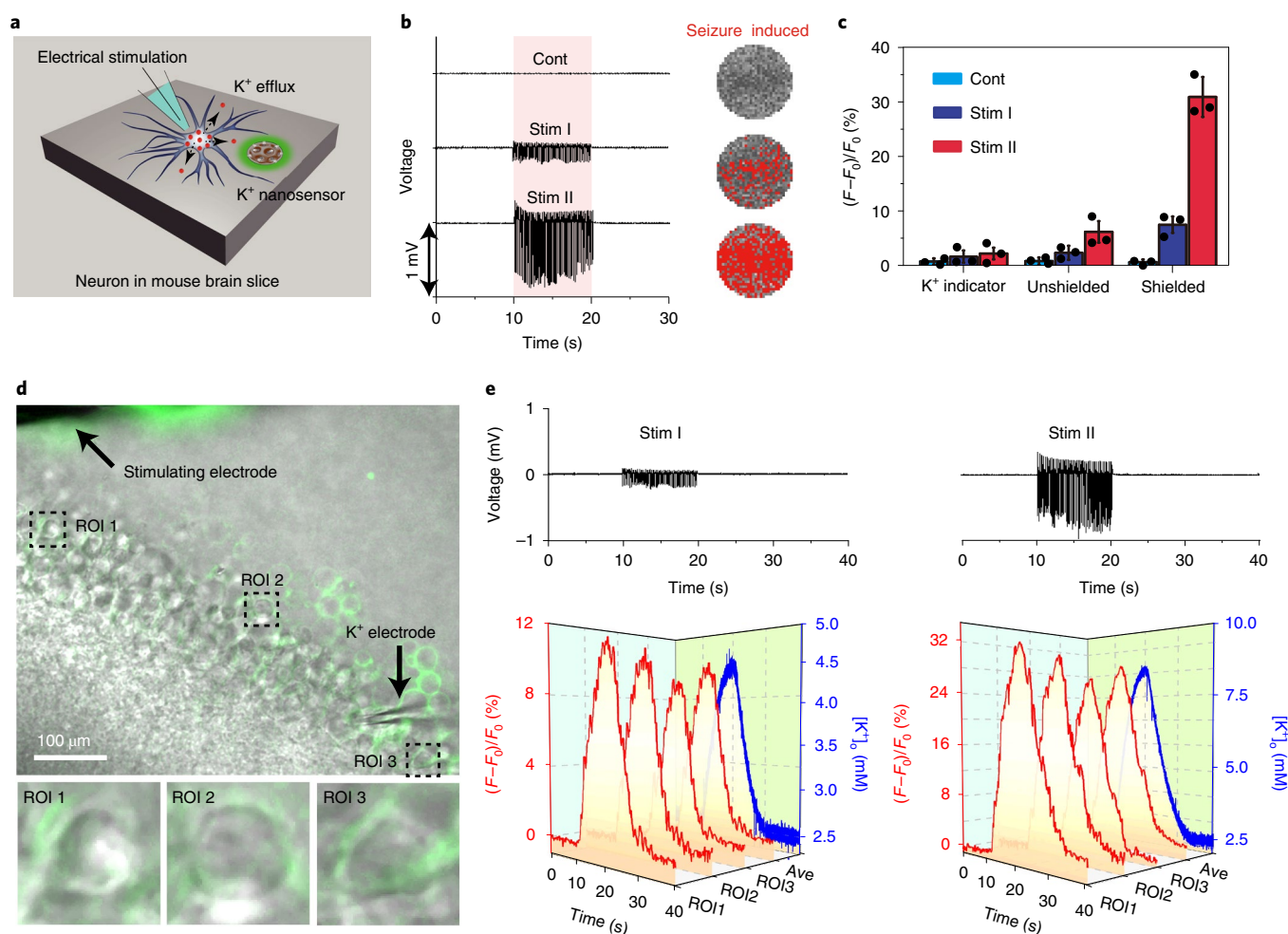
Fig. 4 | Imaging of K⁺ release in brain slices. a, Experimental scheme for imaging electrically evoked K⁺ release in an acute dorsal striatum brain slice. **b**, Extracellular fluorescence responses (right) for the given electrical pulses of different intensities (left). The red dots represent the extracellular regions where the signal responses ($\Delta F/F_0$) are greater than 5%. Cont, control; Stim, stimulation. **c**, Quantification of fold changes in peak fluorescence response in **b** shows that only the shielded nanosensors can detect the $[K^+]_o$ changes in the electrically stimulated brain slices. Data are presented as mean $\pm$ s.e.m. ($n=3$ biologically independent brain slices). **d**, Fluorescent images of brain slices labelled with the shielded nanosensors. **e**, $[K^+]_o$ changes in the brain slices in response to the electrical stimulation were recorded by both K⁺-selective microelectrode (blue line) and optical imaging of the nanosensors (red line). The experiments in **d** and **e** were repeated in three biologically independent brain slices. Ave, the average of signals from ROI 1, ROI 2 and ROI 3.

Eventually, an equilibrium state would require higher $[K^+]_{in}$ than $[K^+]_{out}$ to compensate the electrostatically driven influx with the diffusional outflux. This imbalance between $[K^+]_{in}$ and $[K^+]_{out}$ could be verified by measuring $[K^+]_{in}$ after dispersing the shielded nanosensors to the solutions of varied $[K^+]_{out}$. We found that $[K^+]_{in}$ values were always higher than corresponding $[K^+]_{out}$ values at equilibrium state (Supplementary Fig. 16), reflecting the Gibbs–Donnan effect induced by the negatively charged MSNs[37]. As a result, the negatively charged mesopores in the nanosensors enrich the $[K^+]_{in}$ with respect to the $[K^+]_{out}$ (refs. [38,39]), so that the embedded K⁺ fluorescent indicators can be activated by the magnified $[K^+]$. This feature significantly enhances the sensitivity of the nanosensors.

Spatiotemporal mapping of K⁺ release in neurons

Cultured hippocampal neurons were first preincubated with the shielded K⁺ nanosensors in artificial cerebrospinal fluid (aCSF), and then exposed to *Coriaria* lactone to induce seizure-like activity[40] (Fig. 3a). Inductively coupled plasma atomic emission spectroscopy revealed a trend of increasing $[K^+]_o$ and decreasing $[Na^+]_o$ after the exposure to *Coriaria* lactone (Fig. 3b), of which the sum remained

nearly unchanged. The *Coriaria* lactone-induced $[K^+]_o$ increase could also be detectable by the shielded K⁺ nanosensors. In contrast, no significant change in fluorescent intensity was observed for free indicators and unshielded nanosensors because of their poor selectivity in discriminating Na⁺ and K⁺.

To map the spatial K⁺ release on a single neuron, we modified the surface of the shielded nanosensors with glutathione and cysteamine (designated as Glu/Cys-nanosensors) so that the nanosensors could be anchored on the plasma membrane[41,42]. The Glu/Cys-nanosensors showed similar responses to $[K^+]$ changes as compared with the unmodified ones (Supplementary Fig. 17), and could remain attached to the neuronal membrane in the mouse brain for as long as 1 week (Supplementary Fig. 18). Compared with the control group, the mice injected with the Glu/Cys-nanosensors did not display any discernible neuronal loss (Supplementary Fig. 19). Moreover, there was no obvious immune response in the brain of the mice in which the nanosensors had been injected 1 week before (Supplementary Fig. 20). Electrophysiology study on the brain slices from the nanosensor-treated mice also did not show any significant change in neuronal intrinsic excitability and resting membrane
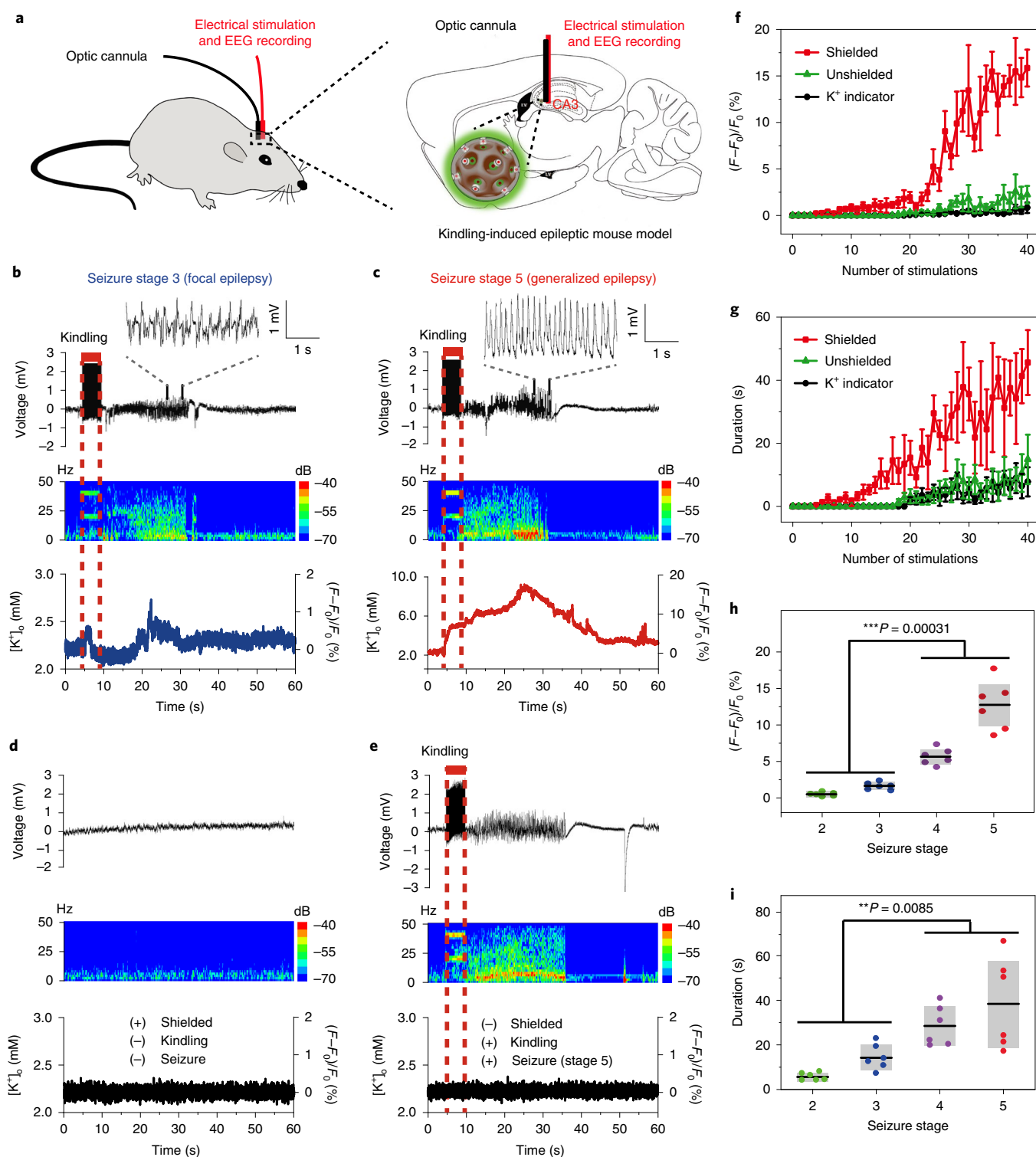
Fig. 5 | Dynamic $[K^+]_o$ fluctuations in the brain of freely moving mice. a, In vivo experimental scheme for $[K^+]_o$ sensing in a kindling-induced epileptic mouse model, in which repeated electrical stimulation increases the seizure severity. **b,c**, Simultaneous neural activity recording and fluorescent imaging of the mice at different epileptic seizure stages (**b**, seizure stage 3; **c**, seizure stage 5). Top, typical EEG data recorded from the subicula during epilepsy and their enlarged views. Middle, corresponding energy spectra for the EEG data. Bottom, fluorescence responses of the sensors to the kindling-induced epileptic seizures at stages 3 and 5. **d**, No fluorescence response in freely moving normal mouse injected with shielded nanosensors. **e**, No fluorescence response in epileptic mouse (seizure stage 5) injected with aCSF. Top, typical EEG data recorded from the subicula. Middle, corresponding energy spectra for the EEG data. Bottom, fluorescence recordings. The experiments for **b**–**e** were repeated in three independent mice. **f,g**, Graphs showing the relationship between the changes in amplitude (**f**) or duration (**g**) of the nanosensor fluorescence signal and the number of stimulations. Data are presented as mean ± s.e.m. (*n* = 6 biologically independent mice). **h,i**, Seizure stage-dependent variation in the amplitude (**h**) and duration (**i**) of the nanosensor fluorescence signal. Data are presented as mean ± s.e.m. (*n* = 6 biologically independent experiments). Statistical significance was calculated by Student's *t*-test (unpaired, two tailed). $^{**}P < 0.01$, $^{***}P < 0.001$.
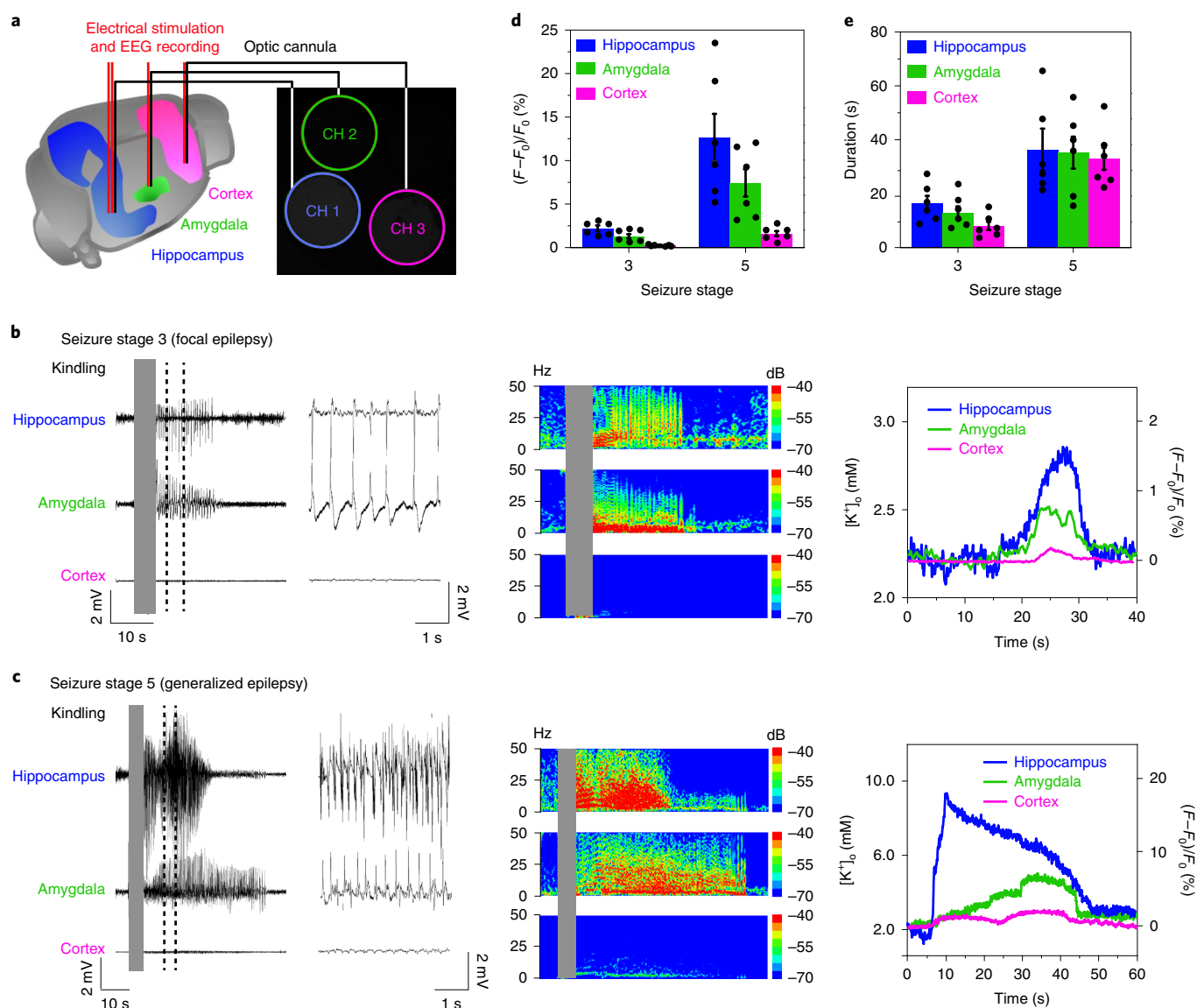
Fig. 6 | Multipoint [K$^+$]$_o$ measurements in freely moving mice. a, Experimental scheme for simultaneous EEG recording and optical [K$^+$]$_o$ sensing in three different brain regions (hippocampus, amygdala and cortex) of the kindling-induced epileptic mouse. **b,c**, On kindling stimulation of the hippocampus that resulted in different degrees of epileptic seizures (**b**, seizure stage 3; **c**, seizure stage 5), both the EEG recording and fluorescent imaging data show various responses in amygdala and cortex. Left, typical EEG data recorded in the hippocampus, amygdala and cortex during the epileptic seizures, and their enlarged views. Middle, corresponding energy spectra for the EEG data. Right, fluorescence responses in three different locations of the mouse epilepsy at different seizure stages. The experiments for **b** and **c** were repeated in three biologically independent mice. **d,e**, Graphs showing the seizure stage-dependent changes in the amplitude (**d**) and duration (**e**) of the nanosensor fluorescence signal in three different locations of the mouse brain. Each group was repeated in three independent mice. Data are presented as mean ± s.e.m. ($n = 6$ biologically independent experiments).

potential (Supplementary Fig. 21). All of these results clearly demonstrated the in vivo biocompatibility of the shielded nanosensors.

The Glu/Cys-nanosensor-labelled hippocampal neurons were cultured in a dual-compartmentalized microchamber, where the axons from the soma compartment grew through the interlinked channels to the axon compartment by 10 d in culture (Fig. 3c). Kainic acid has been shown to acutely induce status epilepticus and recurrent discharges in mice[43]. The representative electroencephalography (EEG) seizure-like activity is shown in Fig. 3d. Kainic acid treatment resulted in periodic seizure-like activities in cultured hippocampal neurons, which were reliably detected by the Glu/Cys-nanosensors anchored to the neuronal membrane (Fig. 3e,f). Compared with the soma, higher [K$^+$]$_o$ was observed in the axons during kainic acid-induced seizure-like activity (Fig. 3e,f), consistent

with the previously reported K$^+$ efflux through voltage-gated K$^+$ channels in the axons to terminate action potentials[44].

We further tested the ability of the shielded K$^+$ nanosensors to detect K$^+$ release in brain slices after applying a brief electrical pulse (Fig. 4a). As expected, the shielded nanosensors detected the [K$^+$]$_o$ change in the electrically stimulated brain slices, whereas the free indicator or unshielded nanosensor did not (Fig. 4b,c). To map the location of the K$^+$ release in the brain slices, we anchored the Glu/Cys-nanosensors onto the surface of neurons and performed simultaneous K$^+$-selective microelectrode recording and optical imaging (Fig. 4d). The microelectrode recording revealed that [K$^+$]$_o$ in the brain slices continuously increased during the electrical stimulation of 10 s, and gradually decreased to the baseline after the termination of the electrical stimulation (Fig. 4e). Similar temporal changes

in $[K^+]_o$ were detected by the shielded nanosensors, demonstrating their effectiveness in measuring $[K^+]_o$ dynamics. Importantly, as the distance between the selected regions of interest and the stimulating electrode increased, the slightly decreased optical signal of $[K^+]_o$ could be observed. Neither the drug treatment nor the current stimulation affected the emission property of the nanosensors (Supplementary Fig. 22). These results indicate the ability of the shielded nanosensors to map the activity-dependent changes in $[K^+]_o$ with high sensitivity and selectivity even in the presence of interferences by Na^+ ions or other confounding factors.

Monitoring potassium levels in hippocampus of epileptic mice

To assess the ability of the nanosensors to report the dynamic changes in $[K^+]_o$ evoked by seizures in vivo, the shielded nanosensors were injected intracranially into the mouse hippocampal CA3 region, which is known to be hyperexcitable during seizures (Fig. 5a). We used the kindling model of epilepsy, in which the daily electrical stimulation of the hippocampus via implanted electrodes for 4 d (ref. [45]) gave rise to more serious seizures in mice as reflected by the increased seizure stages and after-discharge durations (Supplementary Fig. 23).

To examine the K^+ release during the seizures in the kindling model, we simultaneously performed the optical imaging of the shielded nanosensors and EEG recording of neural activity in the hippocampal CA3 region. The optical imaging results were significantly different depending on the seizure intensity ranging from stage 2 to 5 (Fig. 5b,c and Supplementary Fig. 24), as evaluated by the EEG data obtained directly from the epileptogenic zone and epileptic behaviours (Supplementary Videos 3–8). As calculated from the calibration curve (Supplementary Fig. 25), the maximum $[K^+]_o$ in the mice during the generalized seizure reached ~9.2 mM (Fig. 5c). This value is consistent with the inductively coupled plasma measurements of $[K^+]_o$ (8.0 ± 1.9 mM) in the hippocampus after kainic acid-induced status epilepticus.

We did not observe any change in fluorescence signal for the control groups, either in freely moving normal mice injected with the shielded nanosensors (Fig. 5d) or epileptic mice (seizure stage 5) injected with aCSF (Fig. 5e). The mice injected with the shielded nanosensors displayed concurrent increases in both response magnitude and signal duration under continuous kindling stimulations (Fig. 5f,g). Furthermore, both the response magnitude and the signal duration gradually increased as the seizure stages progressed (Fig. 5h,i). In contrast, the mice that received free indicator or unshielded nanosensor treatment did not show any fluorescence response (Fig. 5f,g). These results together indicate that only the shielded nanosensors are sensitive to the $[K^+]_o$ increase caused by the neuronal hyperexcitability.

Multipoint monitoring of potassium levels in epileptic mice

Non-invasive multipoint $[K^+]_o$ measurement will be a useful technique in the neuroscience field for examining the spread of seizures as well as interactions among different brain regions in behaving animals. To further check the ability of the nanosensors for the multipoint measurement of $[K^+]_o$ in freely moving mice, we injected the nanosensors into three different locations of the mouse brains including the hippocampus, amygdala and cortex (Fig. 6a). After the kindling stimulation at the hippocampus, the EEG and optical responses of the nanosensors at the injected locations were simultaneously recorded. For either focal (Fig. 6b) or generalized (Fig. 6c) seizure, obvious increases in $[K^+]_o$ were observed in all three regions, among which the hippocampus showed the largest increase. The magnitude (Fig. 6d) and duration (Fig. 6e) of the $[K^+]_o$ increase in the hippocampus gradually decreased from the amygdala to cortex. Interestingly, a temporal spread in $[K^+]_o$ increases from hippocampus to amygdala and cortex could be observed for focal seizure, while the $[K^+]_o$ increase happens almost at the same time for the

generalized seizure. These results are in good agreement with the widely accepted view that kindling stimulation in hippocampus recruits the adjacent brain area first and that the recruitment propagates throughout the entire brain during kindling acquisition[46].

Conclusions

Our study demonstrates a nanosensor capable of monitoring $[K^+]_o$ dynamics in the interstitial spaces of the acute brain slices and in the brains of freely moving mice. Compared with the invasive K^+-selective microelectrode, which can be used merely for the single-point measurement of $[K^+]$ in a fixed sample, our nanosensors are non-invasive and can convey the spatial information of $[K^+]$ change on a wide scale for freely moving mice. Further development of tissue-penetrating near-infrared emission-based K^+ nanosensors would allow the precise detection of the epileptic foci[47] in the whole-brain imaging, thereby facilitating diagnosis and therapy of epilepsy and decreasing the need for resective surgery in epilepsy. Once loaded with antiepileptic drugs[48,49] and coated with nanocomposites that can be disrupted by elevated $[K^+]_o$, these nanosensors will also enable a highly localized and on-demand drug release at the seizure foci.

Online content

Any methods, additional references, Nature Research reporting summaries, source data, extended data, supplementary information, acknowledgements, peer review information; details of author contributions and competing interests; and statements of data and code availability are available at https://doi.org/10.1038/s41565-020-0634-4.

References

1. Alivisatos, A. P. et al. The brain activity map. *Science* **339**, 1284–1285 (2013).
2. Chung, K. et al. Structural and molecular interrogation of intact biological systems. *Nature* **497**, 332–337 (2013).
3. Chung, K. & Deisseroth, K. Clarity for mapping the nervous system. *Nat. Methods* **10**, 508–513 (2013).
4. Robinson, J. T. et al. Vertical nanowire electrode arrays as a scalable platform for intracellular interfacing to neuronal circuits. *Nat. Nanotechnol.* **7**, 180–184 (2012).
5. Abbott, J. et al. CMOS nanoelectrode array for all-electrical intracellular electrophysiological imaging. *Nat. Nanotechnol.* **12**, 460–466 (2017).
6. Yellen, G. The voltage-gated potassium channels and their relatives. *Nature* **419**, 35–42 (2002).
7. Ding, F. et al. Changes in the composition of brain interstitial ions control the sleep-wake cycle. *Science* **352**, 550–555 (2016).
8. Rasmussen, R. et al. Cortex-wide changes in extracellular potassium ions parallel brain state transitions in awake behaving mice. *Cell Rep.* **28**, 1182–1194 (2019).
9. Kofuji, P. & Newman, E. A. Potassium buffering in the central nervous system. *Neuroscience* **129**, 1045–1056 (2004).
10. Bekar, LaneK. & Nedergaard, M. Is potassium a ubiquitous mediator of vasodilation in the central nervous system? *Biophys. J.* **105**, 2238–2239 (2013).
11. Ammann, D. *Ion-Selective Microelectrodes, Principles, Design and Application* (Springer, 1987).
12. Antonio, L. L. et al. In vitro seizure like events and changes in ionic concentration. *J. Neurosci. Meth.* **260**, 33–44 (2016).
13. Kann, O. et al. Metabolic dysfunction during neuronal activation in the ex vivo hippocampus from chronic epileptic rats and humans. *Brain* **128**, 2396–2407 (2005).
14. Heinemann, U. & Dietzel, I. Extracellular potassium concentration in chronic alumina cream foci of cats. *J. Neurophysiol.* **52**, 421–434 (1984).
15. Hablitz, J. J. & Heinemann, U. Extracellular K^+ and Ca^{2+} changes during epileptiform discharges in the immature rat neocortex. *Dev. Brain Res.* **36**, 299–303 (1987).
16. Yin, J., Hu, Y. & Yoon, J. Fluorescent probes and bioimaging: alkali metals, alkaline earth metals and pH. *Chem. Soc. Rev.* **44**, 4619–4644 (2015).
17. Kim, E. H., Chin, G., Rong, G., Poskanzer, K. E. & Clark, H. A. Optical probes for neurobiological sensing and imaging. *Acc. Chem. Res.* **51**, 1023–1032 (2018).
18. Kong, X. et al. A highly selective mitochondria-targeting fluorescent K^+ sensor. *Angew. Chem. Int. Ed.* **54**, 12053–12057 (2015).

19. Wellbourne-Wood, J., Rimmele, T. S. & Chatton, J.-Y. Imaging extracellular potassium dynamics in brain tissue using a potassium-sensitive nanosensor. *Neurophotonics* **4**, 015002 (2017).
20. Bischof, H. et al. Novel genetically encoded fluorescent probes enable real-time detection of potassium in vitro and in vivo. *Nat. Commun.* **8**, 1422 (2017).
21. Padmawar, P., Yao, X., Bloch, O., Manley, G. T. & Verkman, A. S. K^+ waves in brain cortex visualized using a long-wavelength K^+-sensing fluorescent indicator. *Nat. Methods* **2**, 825–827 (2005).
22. He, H., Mortellaro, M. A., Leiner, M. J. P., Fraatz, R. J. & Tusa, J. K. A fluorescent sensor with high selectivity and sensitivity for potassium in water. *J. Am. Chem. Soc.* **125**, 1468–1469 (2003).
23. Zhou, X. et al. A new highly selective fluorescent K^+ sensor. *J. Am. Chem. Soc.* **133**, 18530–18533 (2011).
24. Rimmele, T. S. & Chatton, J.-Y. A novel optical intracellular imaging approach for potassium dynamics in astrocytes. *PLoS ONE* **9**, e109243 (2014).
25. Burns, A., Ow, H. & Wiesner, U. Fluorescent core-shell silica nanoparticles: towards "lab on a particle" architectures for nanobiotechnology. *Chem. Soc. Rev.* **35**, 1028–1042 (2006).
26. Ma, K., Sai, H. & Wiesner, U. Ultrasmall sub-10 nm near-infrared fluorescent mesoporous silica nanoparticles. *J. Am. Chem. Soc.* **134**, 13180–13183 (2012).
27. Burns, A. A. et al. Fluorescent silica nanoparticles with efficient urinary excretion for nanomedicine. *Nano Lett.* **9**, 442–448 (2009).
28. Wu, W. et al. Enhanced separation of potassium ions by spontaneous K^+-induced self-assembly of a novel metal-organic framework and excess specific cation-π interactions. *Angew. Chem. Int. Ed.* **53**, 10649–10653 (2014).
29. Pauling, L. *The Nature of the Chemical Bond and the Structure of Molecules and Crystals* 3rd edn (Cornell Univ. Press, 1960).
30. Liu, X. et al. Biomimetic DNA nanotubes: nanoscale channel design and applications. *Angew. Chem. Int. Ed.* **58**, 8996–9011 (2019).
31. Meyer, D., Hagemann, A. & Kruss, S. Kinetic requirements for spatiotemporal chemical imaging with fluorescent nanosensors. *ACS Nano* **11**, 4017–4027 (2017).
32. Volkov, A. G., Paula, S. & Deamer, D. W. Two mechanisms of permeation of small neutral molecules and hydrated ions across phospholipid bilayers. *Bioelectrochem. Bioenerg.* **42**, 153–160 (1997).
33. Mancinelli, R., Botti, A., Bruni, F., Ricci, M. A. & Soper, A. K. Hydration of sodium, potassium, and chloride ions in solution and the concept of structure maker/breaker. *J. Phys. Chem. B* **111**, 13570–13577 (2007).
34. Soper, A. K. & Weckström, K. Ion solvation and water structure in potassium halide aqueous solutions. *Biophys. Chem.* **124**, 180–191 (2006).
35. Doyle, D. A. et al. The structure of the potassium channel: molecular basis of K^+ conduction and selectivity. *Science* **280**, 69–77 (1998).
36. Noskov, S. Y., Bernèche, S. & Roux, B. Control of ion selectivity in potassium channels by electrostatic and dynamic properties of carbonyl ligands. *Nature* **431**, 830–834 (2004).
37. Donnas, F. G. The Donnan membrane equilibrium. *Nature* **157**, 495–496 (1946).
38. Gao, J. et al. High-performance ionic diode membrane for salinity gradient power generation. *J. Am. Chem. Soc.* **136**, 12265–12272 (2014).
39. Pu, Q., Yun, J., Temkin, H. & Liu, S. Ion-enrichment and ion-depletion effect of nanochannel structures. *Nano Lett.* **4**, 1099–1103 (2004).
40. Wang, Y. et al. A kindling model of pharmacoresistant temporal lobe epilepsy in Sprague–Dawley rats induced by *Coriaria* lactone and its possible mechanism. *Epilepsia* **44**, 475–488 (2003).
41. Yu, M., Zhou, C., Liu, J., Hankins, J. D. & Zheng, J. Luminescent gold nanoparticles with pH-dependent membrane adsorption. *J. Am. Chem. Soc.* **133**, 11014–11017 (2011).
42. Chen, G. et al. Glutathione-capped quantum dots for plasma membrane labeling and membrane potential imaging. *Nano Res.* **12**, 1321–1326 (2019).
43. Sperk, G. Kainic acid seizures in the rat. *Prog. Neurobiol.* **42**, 1–32 (1994).
44. Lai, H. C. & Jan, L. Y. The distribution and targeting of neuronal voltage-gated ion channels. *Nat. Rev. Neurosci.* **7**, 548–562 (2006).
45. Wang, Y. et al. Depolarized gabaergic signaling in subicular microcircuits mediates generalized seizure in temporal lobe epilepsy. *Neuron* **95**, 92–105 (2017).
46. Bertram, E. H. Neuronal circuits in epilepsy: do they matter? *Exp. Neurol.* **244**, 67–74 (2013).
47. Duncan, J. S. Imaging in the surgical treatment of epilepsy. *Nat. Rev. Neurol.* **6**, 537–550 (2010).
48. Rogawski, M. A. & Löscher, W. The neurobiology of antiepileptic drugs. *Nat. Rev. Neurosci.* **5**, 553–564 (2004).
49. Rogawski, M. A. & Löscher, W. The neurobiology of antiepileptic drugs for the treatment of nonepileptic conditions. *Nat. Med.* **10**, 685–692 (2004).

Methods

Materials. All commercially obtained chemicals were used without further purification. Hexadecyltrimethylammonium chloride (CTAC) (25 wt%), triethanolamine, tetraethyl orthosilicate, sodium chloride (NaCl), potassium carbonate, dimethyl sulfoxide, 1-ethyl-3-(3-dimethly-aminopropyl) carbodiimide (EDC), *N*-hydroxysuccinimide (NHS), glutathione and cysteamine were purchased from Sigma-Aldrich. Ethanol, methonal, dimethylformamide and acetonitrile were purchased from Samchun Chemical. APG was purchased from Abcam. Amine-terminated poly(ethylene glycol) (weight-averaged molecular mass (M_w) = 5,000) was purchased from Nanocs. DMEM, fetal bovine serum (FBS) and PBS were provided by Gibco BRL (Invitrogen).

Cell culture. HEK 293 cell lines were purchased from the Cell Bank of Type Culture Collection of the Shanghai Institute of Cell Biology, Chinese Academy of Sciences, where they were characterized systematically by DNA fingerprinting, isozyme detection and mycoplasma detection. They were grown in monolayers in DMEM supplemented with 10% heat-inactivated FBS at 37 °C under a humidified 5% CO_2 atmosphere.

We prepared hippocampal neuronal cultures using postnatal day 0 Sprague–Dawley rat pups (male) according to a previously reported standard method[50]. Firstly, neurons were cultured at 50,000 cells per cm^2 on a 1-cm glass coverslip coated with matrigel (BD Biosciences). The culture medium (1 ml) contained Neurobasal medium (Invitrogen), B-27 (Invitrogen), 2 mM Glutamax-I (Invitrogen) and 2.5% FBS. After astrocytes sufficiently proliferated and formed a monolayer on the entire coverslip, we treated the cells with mitotic inhibitor 5-fluoro-2'-deoxyuridine (Sigma). All in vitro/ex vivo/in vivo experiments were approved by the Zhejiang University Animal Experimentation Committee and were in complete compliance with the National Institutes of Health *Guide for the Care and Use of Laboratory Animals*.

Synthesis of filter membrane-shielded nanosensors. The MSNs were synthesized using the procedures from the literature with some modifications[51]. CTAC (2 g) and triethanolamine (0.07 g) were dissolved in deionized water (20 ml) under vigorous stirring. Then, the temperature was increased to 95 °C. After stabilization for 1 h, 1.5 ml of tetraethyl orthosilicate was added dropwise within 2 min. The mixed solution was kept at 95 °C for another 1 h with magnetic stirring (400 r.p.m.). Subsequently, the nanoparticles were obtained by centrifugation (15,000 r.p.m., 15 min) and washed three times with ethanol. To extract the template CTAC, the collected nanoparticles were dialysed with a 1 wt% solution of NaCl in methanol for 3 h at room temperature. The CTAC-removed MSNs can be easily dispersed in deionized water for further use.

To load APG into the mesopores of MSNs, 1 ml of MSNs (50 mg) and 10 ml of 0.5 mg ml^{-1} APG in deionized water were mixed and the suspension was stirred in the dark for 24 h at room temperature. The resulting nanoparticles (MSN-APG) were collected by centrifugation and washed with deionized water three times.

Filter membrane precursors were prepared as follows: 3.4 g of N-benzylsalicylamide and 2.5 g of anhydrous potassium carbonate were added into 25 ml of anhydrous dimethylformamide. The resulting mixture was heated to 90 °C. Subsequently, 2.9 g of 1,1,1-tris(p-tosyloxy-methyl)ethane and 0.3 ml of 2-aminoterephthalic acid were added into the solution and the mixture was stirred for 12 h. After cooling down to the room temperature, 200 ml of deionized water was added into the reaction mixture. By using petroleum ether-ethylacetate as eluent (v/v = 2:1), the resulting solid products were treated by column chromatography on silica gel to furnish the precursor as a white solid.

By an in situ loading procedure, the filter membrane precursor was deposited onto the surface of MSN-APG directly in an acetonitrile solution. Specifically, a 10-ml acetonitrile solution containing 1 mg of filter membrane precursor was added into a 50-ml acetonitrile ultrasonic suspension of MSN-APG (50 mg) under vigorous stirring. The mixture was kept at 50 °C for 10, 20, 40 and 60 min, which resulted in the generation of the nanosensors with shell thicknesses of ~1.5, ~3.5, ~10 and ~17 nm, respectively. After annealing at room temperature for 12 h, the obtained nanosensors were washed with methanol once and then water twice, and finally dispersed in 10 ml of deionized water.

Surface modification of nanosensors with both glutathione and cysteamine. The surface of filter membrane-shielded nanosensors was modified with glutathione and cysteamine to target the cell membrane. Briefly, the filter membrane-shielded nanosensors (1 mg ml^{-1}) were activated with EDC/NHS (10 mM EDC and 10 mM NHS) for 30 min in deionized water at pH 5.6. Then 1 ml of water solution containing both reduced L-glutathione (12.5 mM) and cysteamine (12.5 mM) was added. After incubating the mixed solution at room temperature for 30 min, excessive glutathione and cysteamine were removed by centrifugation at 13,000 r.p.m. for 20 min. The obtained nanoparticles were washed with ethanol twice and dispersed in deionized water.

Molecular dynamics simulations to demonstrate the selectivity of the filter membrane. The restrained electrostatic potential charge of the filter membrane was calculated by Gaussian 03 with the Hartree–Fork method using 6–31 + G(d) basis set[52]. Then, the restrained electrostatic potential charge was used as a charge method to generate a general Amber force field by AmberTools[53]. The parameters for the solvents and ions were obtained from Amber 03 Force Field.

The box used for the simulation was set as $6 \times 6 \times 13$ nm^3 to fit the size of the filter membrane and water environment, with the filter membrane layer positioned at the centre of the box. Simple point charge water model was added as a solvent to fill the box, 20 K^+/Na^+ ions were placed above the filter membrane layer in water and 20 Cl^- ions were placed below the filter membrane layer to equilibrate the charge of the system. Then, the construction of the system model was completed, and the molecular visualization could be obtained by using visual molecular dynamics (VMD) graphics software[54].

After the construction of the model, 10-ns molecular dynamics simulation was conducted. The simulation system was set as an isothermal-isobaric ensemble system, and *x* and *y* axis directions were in periodic boundary conditions. The temperature of the system was set at 298 K and the pressure was 1 bar. The time step was set as 2 fs per step. With the simulation running, we calculated the electrostatic interactions by using the particle mesh Ewald method[55]. In addition, the Lennard-Jones potential for the cross-interactions among the non-bonded atoms was calculated by the Lorentz–Berthelot rule[56]. The cut-off of particle mesh Ewald and van der Waals interactions was set as 1.2 nm.

3-(4,5-dimethyl-2-thiazolyl)-2,5-diphenyl-2-H-tetrazolium bromide assay. To test the cytotoxicity of nanosensors, the HEK 293 cells were cultured with varied concentrations of nanosensor (5, 10, 20, 50 and 100 μg ml^{-1}) for different time durations (6, 12, 24, 36 and 48 h). Afterwards, 100 μl of culture medium containing 50 μg of 3-(4,5-dimethyl-2-thiazolyl)-2,5-diphenyl-2-H-tetrazolium bromide was added in each well. After 4 h of incubation, the cultured medium was extracted and 100 μl of dimethyl sulfoxide was added per well. The absorbance at 490 nm was measured by a multiple plate reader (Bio-TekELx800).

Elemental quantification of $[K^+]_o$. At 14 d in vitro, primary hippocampal neurons (1×10^8) were dissociated from the culture plates via trypsin and incubated with 1 ml of aCSF (in mM: 119 NaCl, 26.2 NaHCO$_3$, 11 D-glucose, 2.5 KCl, 2.5 CaCl$_2$, 1.3 MgSO$_4$ and 1 NaH$_2$PO$_4$) containing both nanosensors (20 μg ml^{-1}) and *Coriaria* lactone (100 μM). The media were collected at different time points (from 0 to 30 min) after the *Coriaria* lactone incubation and the concentrations of K^+ were detected by inductively coupled plasma atomic emission spectroscopy. Finally, $[K^+]_o$ at different incubation time points was calculated.

Confocal laser scanning microscopy (CLSM) imaging of the hippocampal neurons in the compartmentalized neuron culture system. The compartmentalized culture device obtained from Xona (SND450) includes two rectangular compartments that are interconnected by several parallel microchannels. The microchannels are too narrow to allow the transport of the somas but are wide enough to allow the natural extension of the axons[57]. As a result, this device can be used to spatially isolate the axons from the somas. For imaging experiments, we used an inverted fluorescence microscope (Olympus, FV 1000) equipped with a ×20 water immersion objective lens. The hippocampal neurons at 10 d in vitro were treated with 400 μl of aCSF containing the Glu/Cys-nanosensors (20 μg ml^{-1}). After incubation for 20 min, the neurons were treated with 400 μl of fresh aCSF and then visualized with the CLSM in real-time for 5 min. Subsequently, the neurons were treated with 400 μl of aCSF containing 5 or 10 μM kainic acid and then visualized with the CLSM in real-time for another 15 min.

Mice and brain slices. Healthy C57/BL6 mice (male, 2–4 months) were used in all ex vivo and in vivo experiments. These mice of normal immune status were not treated with any drugs or previous tests. Before surgery, the mice were kept in groups within cages. They had free access to food and water, and were allowed to experience 12-h light/dark cycles (lights on during 8:00 to 20:00). After surgery, they were housed individually. We conducted all behavioural/imaging experiments during 9:00 to 18:00.

To obtain acute hippocampal slices, we decapitated C57/BL6 mice (postnatal day 10–14) and quickly removed the brain. The brain was then submerged in aCSF at 4 °C saturated with mixed gas containing 95% O$_2$ and 5% CO$_2$. The hippocampal slices (300 μm in thickness) were cut using a vibratome (VT1000S, Leica instruments) and kept in oxygenated aCSF at 25 °C. To induce epileptiform discharge ex vivo, an isolated stimulator (ISO-Flex, A.M.P.I. Instruments) was used. The stimulating electrode (bipolar stereotrodes, MicroProbes) was placed in the CA1 region. The stimulating parameter was 50 Hz, pulse width was 10 ms and intensity was 100 and 500 μA. Glass pipettes (200–500 kΩ) were pulled from glass capillaries on a two-stage puller (PC-10, Narishige) and filled with aCSF. To record the evoked epileptiform discharges, the pipettes were placed near the stimulating electrode (at approximately 200 μm) in CA1.

Optical imaging and microelectrode recording in the brain slices. The labelling of the nanosensors in the brain slices was achieved by incubating the brain slices with 2 ml of aCSF containing the glutathione- and cysteamine-modified nanosensors ($20\,\mu g\,ml^{-1}$) for 20 min. K^+-sensitive microelectrodes were prepared as previously described[58]. In brief, pipettes were treated with dimethyldichlorosilane (Silanization Solution I, Sigma-Aldrich) for silanization and loaded with K^+ exchanger (potassium ionophore I-cocktail A, Sigma-Aldrich) at 100- to 150-μm column diameter and then refilled with 100 mM KCl. The reference and K^+ signals were amplified and displayed on a chart recorder. Before the experiments, the electrode calibration was performed with 2.5–50 mM K^+ in aCSF for each experiment. Recordings in the slices were made 50–100 μm below the slice surface during the whole hippocampal stimulation period.

In vitro electrophysiology. To test whether the nanosensors would affect electrophysiological properties of the neurons, we prepared acute hippocampal slices from the mice in which aCSF ($1\,\mu l$) or the nanosensors ($20\,\mu g\,ml^{-1}$, $1\,\mu l$) were injected 7 d before. Whole-cell patch-clamp recordings were performed in voltage-clamp configuration while holding the neurons at -60 mV throughout the experiment using an EPC10 patch-clamp amplifier (HEKA Instruments), with a low-pass filter at 3 kHz and a sample rate of 1 kHz. The tip resistances of the recording electrodes were ~4–8 MΩ. Recording pipettes were routinely filled with a solution containing the following (in mM): 140 K-gluconate, 5 NaCl, 2 Mg-ATP, 0.2 EGTA and 10 HEPES. A series of 500-ms depolarizing current pulses (increased in 20-pA steps) were applied to measure the firing properties of the neurons with or without the labelling of the nanosensors.

Hippocampal kindling. On intraperitoneal injection of sodium pentobarbital at the dosage of $50\,mg\,kg^{-1}$ for anaesthesia, we mounted the mice in a stereotaxic apparatus (512600, Stoelting) and implanted a home-made cannula-electrode (electrode: 0.125 mm in diameter, 795500; cannula: 62003, RWD Life Science). Both cannula and electrode were located directly into the right ventral hippocampus (anteroposterior (AP) $=-2.9$ mm, lateral (L) $=-3.0$ mm, ventral (V) $=-3.2$ mm) for the convenience of EEG recording, kindling stimulation and intra-hippocampal injection of nanosensors. We kept the location of the cannula ~0.5 mm above the tips of electrode for optimal imaging. We placed two screws over the cerebellum and another screw over the sensorimotor cortex because they not only secured the dental cement but also served as ground electrodes and the reference. After kindling stimulations, we histologically confirmed the locations of the electrodes. Only the mice with the correct electrode locations were taken into analysis.

After 7-d recovery, a stimulator with constant current (SEN-7203 and SS-202J, Nihon Kohden) was used to determine the after-discharge threshold of every mouse (monophasic square-wave pulses, 20 Hz, 1 ms per pulse, 40 pulses). EEG was recorded by a PowerLab system (AD Instruments). We stimulated the mice with the starting intensity at $40\,\mu A$, which was gradually increased in 20-μA steps every 1 min. We defined the after-discharge threshold as the minimum intensity that could trigger more than 5 s of after-discharge duration. Such an intensity was used for the subsequent experiments. Afterwards, all mice received ten times the kindling stimulations ($400\,\mu A$, 20 Hz, 2-s trains, 1-ms monophasic square-wave pulses) daily. Seizure stages were classified based on the Racine scale[59]: stage 1, facial movement; stage 2, head nodding; stage 3, unilateral forelimb clonus; stage 4, bilateral forelimb clonus and rearing; and stage 5, rearing and falling. Stages 1–3 and 4–5 were classified as the local seizures and the generalized seizures, respectively[60].

Simultaneous hippocampal kindling and optical imaging. We injected the shielded nanosensors (intra-hippocampal injection, $20.0\,\mu g\,ml^{-1}$, $1\,\mu l$) every day 30 min before the kindling. For control experiments, unshielded nanosensors (intra-hippocampal injection, $14.8\,\mu g\,ml^{-1}$, $1\,\mu l$) or free indicators (intra-hippocampal injection, $0.8\,\mu g\,ml^{-1}$, $1\,\mu l$) were injected. We delivered a blue laser light (488 nm) source by an optical fibre (200 μm in diameter), which was connected to the fibre photometry system (OBIS 488LS, Nanjing Thinkertech). The optical fibre was trimmed to be smooth and flat in advance. After removing the stylet from the guide cannula, we directly inserted the optical fibre into the regions above the hippocampus. After mice were placed in the chamber, we secured the optical fibre to ensure no dislocation during the epileptic seizures. During the whole process of kindling stimulation, optical imaging was simultaneously performed. All experiments were performed at the laser power of 5.0 mW.

For simultaneous multipoint optical imaging of $[K^+]_o$ in the brains of the freely moving mice, we implanted the cannula-electrodes into the right ventral hippocampus (AP $=-2.9$ mm, L $=-3.0$ mm, V $=-3.2$ mm), the left amygdala (AP $=-1.8$ mm, L $=+3.0$ mm, V $=-4.8$ mm) and sensorimotor cortex (AP $=+1.5$ mm, L $=+1.5$ mm, V $=-2.0$ mm). The shielded nanosensors ($20\,\mu g\,ml^{-1}$, $1\,\mu l$) were injected into each brain region 30 min before the kindling stimulation. The EEG and optical imaging (Inper fibre photometry system) data were simultaneously collected in three regions.

Immunohistochemistry. At 7 d after the injection of aCSF ($1\,\mu l$) or shielded nanosensors ($20\,\mu g\,ml^{-1}$, $1\,\mu l$), mice were deeply anesthetized by intraperitoneal injection of pentobarbital sodium at the dosage of $100\,mg\,kg^{-1}$. Subsequently, they were successively perfused with saline with 4% paraformaldehyde. After removing the brains, fixation was carried out by immersion in 4% paraformaldehyde for 24 h. Following 48 h of dehydration using 30% sucrose, coronal sections were cut with 30-μm thickness on a sliding freezing microtome (CM 3050S, Leica). To identify neurons and glia, we incubated the brain slices firstly in 0.1% Triton X-100 for 15 min to promote perforation and then in 5% donkey serum for 2 h. After the addition of the primary antibodies for neuronal marker NeuN (MABN140, Millipore), excitatory neuronal marker CaMKIIa (Abcam ab92332), GABAergic neuronal marker GAD65/67 (Millipore AB1511), astrocyte marker GFAP (BA0056, Boster) and microglia marker Iba-1 (Abcam, ab178846), the slices were incubated with Alexafluor 594 secondary antibodies. The positively stained cells could be visualized by detecting the fluorescent signal of the secondary antibodies.

Statistical analyses. All data are presented as mean $\pm$ s.e.m. and statistical analyses and graphs were performed using OriginLab 8.5. For comparison of two groups, significance was determined by the two-tailed unpaired Student's t-test. The statistical analyses were carried out with IBM SPSS Statistics 24.

Reporting Summary. Further information on research design is available in the Nature Research Reporting Summary linked to this article.

Data availability
The data that support the plots within this paper and other findings of this study are available from the corresponding author upon reasonable request.

References
50. Meberg, P. J. & Miller, M. W. Culturing hippocampal and cortical neurons. *Methods Cell Biol.* **71**, 111–127 (2003).
51. Pan, L. et al. Nuclear-targeted drug delivery of TAT peptide-conjugated monodisperse mesoporous silica nanoparticles. *J. Am. Chem. Soc.* **134**, 5722–5725 (2012).
52. Frisch, M. J. et al. *Gaussian 03, Revision C.02* (Gaussian, Inc., 2004).
53. Wang, J., Wang, W., Kollman, P. A. & Case, D. A. Antechamber: an accessory software package for molecular mechanical calculations. *J. Am. Chem. Soc.* **222**, U403 (2001).
54. Humphrey, W., Dalke, A. & Schulten, K. VMD: visual molecular dynamics. *J. Mol. Graph. Model.* **14**, 33–38 (1996).
55. Darden, T., York, D. & Pedersen, L. Particle mesh Ewald: an $N\cdot\log(N)$ method for Ewald sums in large systems. *J. Chem. Phys.* **98**, 10089–10092 (1993).
56. Hirschfelder, J. O., Cur- tiss, C. F. & Bird, R. B. *Molecular Theory of Gases and Liquids* 2nd edn (John Wiley & Sons, 1954).
57. Taylor, A. M. et al. A microfluidic culture platform for CNS axonal injury, regeneration and transport. *Nat. Methods* **2**, 599–605 (2005).
58. Xiong, Z.-Q. & Stringer, J. L. Sodium pump activity, not glial spatial buffering, clears potassium after epileptiform activity induced in the dentate gyrus. *J. Neurophysiol.* **83**, 1443–1451 (2000).
59. Racine, R. J. Modification of seizure activity by electrical stimulation: II. Motor seizure. *Electroen. Clin. Neuro.* **32**, 281–294 (1972).
60. Sato, M., Racine, R. J. & McIntyre, D. C. Kindling: basic mechanisms and clinical validity. *Electroen. Clin. Neuro.* **76**, 459–472 (1990).

Acknowledgements

Author contributions
J.L. and D.L. conceived and designed the experiments. J.L. and L.P. fabricated K^+ nanosensors. F.L., L.P., P.L., H.L., G.K., Y.D., K.S., D.K. and J.N. contributed to the nanosensor characterization and data analyses. H.T. carried out high-resolution TEM

Additional information

Supplementary information is available for this paper at https://doi.org/10.1038/s41565-020-0634-4.

Correspondence and requests for materials should be addressed to Z.C., T.H. or D.L.

Peer review information *Nature Nanotechnology* thanks Christophe Bernard and the other, anonymous, reviewer(s) for their contribution to the peer review of this work.

Reprints and permissions information is available at www.nature.com/reprints.

nature research

Corresponding author(s):	Daishun Ling, Taeghwan Hyeon, and Zhong Chen.
Last updated by author(s):	Dec 11, 2019

Reporting Summary

Nature Research wishes to improve the reproducibility of the work that we publish. This form provides structure for consistency and transparency in reporting. For further information on Nature Research policies, see Authors & Referees and the Editorial Policy Checklist.

Statistics

For all statistical analyses, confirm that the following items are present in the figure legend, table legend, main text, or Methods section.

n/a	Confirmed	
☐	☒	The exact sample size (n) for each experimental group/condition, given as a discrete number and unit of measurement
☐	☒	A statement on whether measurements were taken from distinct samples or whether the same sample was measured repeatedly
☐	☒	The statistical test(s) used AND whether they are one- or two-sided *Only common tests should be described solely by name; describe more complex techniques in the Methods section.*
☒	☐	A description of all covariates tested
☒	☐	A description of any assumptions or corrections, such as tests of normality and adjustment for multiple comparisons
☐	☒	A full description of the statistical parameters including central tendency (e.g. means) or other basic estimates (e.g. regression coefficient) AND variation (e.g. standard deviation) or associated estimates of uncertainty (e.g. confidence intervals)
☐	☒	For null hypothesis testing, the test statistic (e.g. F, t, r) with confidence intervals, effect sizes, degrees of freedom and P value noted *Give P values as exact values whenever suitable.*
☒	☐	For Bayesian analysis, information on the choice of priors and Markov chain Monte Carlo settings
☒	☐	For hierarchical and complex designs, identification of the appropriate level for tests and full reporting of outcomes
☒	☐	Estimates of effect sizes (e.g. Cohen's d, Pearson's r), indicating how they were calculated

Our web collection on statistics for biologists contains articles on many of the points above.

Software and code

Policy information about availability of computer code

Data collection	EEG was recorded a using a PowerLab system (AD Instruments, Australia). In vitro electrophysiology was performed by using an EPC10 patch-clamp amplifier (HEKA Instruments; Germany). In vivo K+ optical imaging was recorded with a fiber photometry system (OBIS 488LS, Nanjing Thinkertech). Confocal images were captured with Olympus DP70.
Data analysis	Statistical comparisons were performed using SPSS (version 17.0) or Prism (version 7.0).

For manuscripts utilizing custom algorithms or software that are central to the research but not yet described in published literature, software must be made available to editors/reviewers. We strongly encourage code deposition in a community repository (e.g. GitHub). See the Nature Research guidelines for submitting code & software for further information.

Data

Policy information about availability of data

All manuscripts must include a data availability statement. This statement should provide the following information, where applicable:
- Accession codes, unique identifiers, or web links for publicly available datasets
- A list of figures that have associated raw data
- A description of any restrictions on data availability

All associated raw data is provided in the supplementary information.

Field-specific reporting

Please select the one below that is the best fit for your research. If you are not sure, read the appropriate sections before making your selection.

☒ Life sciences ☐ Behavioural & social sciences ☐ Ecological, evolutionary & environmental sciences

For a reference copy of the document with all sections, see nature.com/documents/nr-reporting-summary-flat.pdf

Life sciences study design

All studies must disclose on these points even when the disclosure is negative.

Sample size	The experiments were done in repeats as stated. Usually 3 repeats as is common in similar experiments. These sample sizes were chosen without sample-size calculations.
Data exclusions	In kindling experiments, only those mice with the correct electrode locations were taken into analysis.
Replication	All experimental findings, including TEM images, emission spectra, and behavioral experiments were reliably reproduced.
Randomization	In the hippocampal kindling model, the initial ADT of each mouse was used for grouping to match their initial epileptogenic sensibility (see Method section: Hippocampal kindling model). In the other experiments, since there were very limited variations which had been confirmed by our previous studies, no statistical methods were used to randomize.
Blinding	Investigators were not blinded for nanomaterial synthesis. However, for in vivo tests, a trained observer who was unaware of the experimental groupings scored the seizure severity and analyzed the data.

Behavioural & social sciences study design

All studies must disclose on these points even when the disclosure is negative.

Study description	*Briefly describe the study type including whether data are quantitative, qualitative, or mixed-methods (e.g. qualitative cross-sectional, quantitative experimental, mixed-methods case study).*
Research sample	*State the research sample (e.g. Harvard university undergraduates, villagers in rural India) and provide relevant demographic information (e.g. age, sex) and indicate whether the sample is representative. Provide a rationale for the study sample chosen. For studies involving existing datasets, please describe the dataset and source.*
Sampling strategy	*Describe the sampling procedure (e.g. random, snowball, stratified, convenience). Describe the statistical methods that were used to predetermine sample size OR if no sample-size calculation was performed, describe how sample sizes were chosen and provide a rationale for why these sample sizes are sufficient. For qualitative data, please indicate whether data saturation was considered, and what criteria were used to decide that no further sampling was needed.*
Data collection	*Provide details about the data collection procedure, including the instruments or devices used to record the data (e.g. pen and paper, computer, eye tracker, video or audio equipment) whether anyone was present besides the participant(s) and the researcher, and whether the researcher was blind to experimental condition and/or the study hypothesis during data collection.*
Timing	*Indicate the start and stop dates of data collection. If there is a gap between collection periods, state the dates for each sample cohort.*
Data exclusions	*If no data were excluded from the analyses, state so OR if data were excluded, provide the exact number of exclusions and the rationale behind them, indicating whether exclusion criteria were pre-established.*
Non-participation	*State how many participants dropped out/declined participation and the reason(s) given OR provide response rate OR state that no participants dropped out/declined participation.*
Randomization	*If participants were not allocated into experimental groups, state so OR describe how participants were allocated to groups, and if allocation was not random, describe how covariates were controlled.*

Ecological, evolutionary & environmental sciences study design

All studies must disclose on these points even when the disclosure is negative.

Study description	*Briefly describe the study. For quantitative data include treatment factors and interactions, design structure (e.g. factorial, nested, hierarchical), nature and number of experimental units and replicates.*
Research sample	*Describe the research sample (e.g. a group of tagged Passer domesticus, all Stenocereus thurberi within Organ Pipe Cactus National Monument), and provide a rationale for the sample choice. When relevant, describe the organism taxa, source, sex, age range and*